



Electronic structure tailoring of Al^{3+} - and Ta^{5+} -doped CeO_2 for the synergistic removal of NO and chlorinated organics

Lu Wei ^{a,b}, Yuxi Liu ^a, Hongxing Dai ^a, Suping Cui ^b, Can Wang ^c, Hsing-Cheng Hsi ^d, Erhong Duan ^e, Yue Peng ^f, Jiguang Deng ^{a,*}

^a Key Laboratory of Beijing on Regional Air Pollution Control, Beijing Key Laboratory for Green Catalysis and Separation, Center of Excellence for Environmental Safety and Biological Effects, Beijing University of Technology, Beijing 100124, China

^b Faculty of Materials and Manufacturing, Key Laboratory of Advanced Functional Materials, Ministry of Education, Beijing University of Technology, Beijing 100124, China

^c School of Environmental Science and Engineering, Tianjin University, Tianjin 300350, China

^d Graduate Institute of Environmental Engineering, National Taiwan University, Taipei 10617, Taiwan

^e School of Environmental Science and Engineering, Hebei University of Science and Technology, 26th Yuxiang Street, Shijiazhuang, Hebei 050018, China

^f State Key Joint Laboratory of Environment Simulation and Pollution Control, School of Environment, Tsinghua University, Beijing 100084, China



ARTICLE INFO

Keywords:

NO
CVOCs
Active site regulation
 CeO_2 based catalyst
Synergistic degradation

ABSTRACT

Balancing the NH_3 selective catalytic reduction (NH₃-SCR) and catalytic oxidation performance is difficult but necessary for the synergistic elimination of NO_x and chlorine-containing volatile organic compounds (CVOCs). We herein unveiled that electronic structure tailoring of the applied catalyst was an efficient pathway for balancing the catalytic behaviors in the NH₃-SCR of NO and chlorobenzene catalytic oxidation (CBCO). Specifically, environmentally friendly CeO_2 substituted by low valent Al^{3+} exhibited better NH₃-SCR of NO and CBCO activity in comparison with the CeO_2 sample without doping. Detailed characterizations and theoretical simulations revealed that the strong dopant-oxide pairs in the CeO_2 with Al^{3+} doping significantly tailored the electronic structure of O 2p states, enhancing the amount of Lewis acid sites and promoting the ability of lattice oxygen to act as an oxidizing agent, thereby leading to superior performance for the synergistic elimination of NO/CB. The counterpart with substitution of high valent Ta^{5+} showed an opposite trend, due to that Ta^{5+} donated more electrons to the coordination oxygen than Ce^{4+} inhibiting lattice oxygen separating from the surface of the catalyst, and Lewis base sites were formed.

1. Introduction

For industries such as municipal solid waste incineration, iron ore sintering, and metal smelting, the tail gas contains both NO_x and chlorine-containing volatile organic compounds (CVOCs), among which CVOCs are mainly polychlorinated homologs and dioxins [1–3]. In the same fixed emission source, it is not advisable to establish a separate CVOCs control unit in terms of cost-effectiveness [4]. Selective catalytic reduction (SCR) and catalytic oxidation (CO) are efficient NO_x and CVOCs removal technologies, respectively [5–7]. Catalyst with high redox performance is the core of the two technologies [8–10]. It is expected that the synergistic elimination of NO_x and CVOCs in the same reactor can be achieved by rational design of double-effect catalysts with catalytic reduction and catalytic oxidation capacities.

The reaction mechanism of NH₃-SCR was still controversial. The widely accepted view was that the reaction follows the Eley-Rideal mechanism, including acid cycle (NH₃ adsorption) and redox cycle (NH₃ activation), which were determined by the acidity and redox capacity of the active site of the catalyst, respectively [11]. Acidic property was associated with the adsorption of NH₃, and redox behavior was necessary to ensure the SCR reaction by oxidizing the NH₂ species [12]. Different catalyst systems have different matching degrees of acidity and redox, resulting in different active intermediates of NH_x/NO_x , which determine the reaction path and reaction efficiency [13–15]. For the catalytic oxidation reaction of CVOCs, the generally accepted mechanism was the Mars-van Krevelen (MvK) mechanism, in which adsorbed CVOCs molecules was oxidized by lattice oxygen on the surface of the catalyst, and the oxidized products were desorbed, leaving oxygen

* Corresponding author.

E-mail address: jgdeng@bjut.edu.cn (J. Deng).

vacancies, and then the surface was reoxidized by gaseous oxygen [16, 17]. Relevant studies have emphasized the synergistic effect of catalyst acidity and oxidation in the catalytic combustion of CVOCs over the composite oxides, transition metals, or rare earth element doped oxides catalysts [18–20]. The strong acid sites in the catalyst can quickly remove surface chlorine species, reducing the formation of organic byproduct [21]. The catalyst with better redox ability can promote degradation of COVCs [22]. Therefore, no matter for NO_x catalytic reduction or CVOCs catalytic oxidation, the acidity and redox properties of the catalyst active site determined by the coordination environment play a decisive role in the activity, selectivity, and stability of the catalyst.

Metal oxide catalysts play a significant role in heterogeneous catalysis that aims to reduce the industrial pollution [23]. The pollutant conversion or product selectivity over the metal oxide catalysts could be improved by substituting with a different cation [24, 25]. However, the improvement of doped oxide catalysts is usually an empirical process, and the catalyst designed by theoretical guidance remains extremely rare [26]. The active sites in such a system could be either the dopant/host cation or the oxygen ion surrounding the dopant/host [27–29]. In this work, considering V, W, and Ti in the commercial $\text{V}_2\text{O}_5\text{-WO}_3\text{-TiO}_2$ catalyst were included in the European Waste Catalogue and Hazardous Waste List, environmentally friendly CeO_2 was selected as the host oxide, and the type and quantity of active sites in CeO_2 were regulated by doping with different valent cations. To gain insights into the regulation mechanism of the active site via substitutional doping, the interaction between the active sites of doped CeO_2 catalyst and the reactive molecules in the synergistic removal of $\text{NO}_x\text{/CVOCs}$ was investigated through experimental and computational methods.

2. Experiment

2.1. Catalyst preparation

All the catalysts in this work were synthesized by the co-precipitation method, and the solid salts were precipitated by evaporating the solvent. Al and Ta were trivalent and pentavalent because the stable oxide was Al_2O_3 and Ta_2O_5 , respectively. Therefore, Al^{3+} and Ta^{5+} were chosen as low-valence substitution and high-valence substitution. Cerium (III) nitrate hexahydrate, aluminum (III) chloride, and tantalic (V) chloride was used as the precursor of Ce, Al, and Ta, respectively. Cerium (III) nitrate hexahydrate was dissolved in deionized water at 80 °C for 3 h under vigorous stirring. Then, the solution was kept in a vacuum drying oven at 70 °C for 12 h. After throughout drying, the as-obtained powder was calcined at 400 °C in a muffle furnace for 6 h to get CeO_2 . The catalyst was marked as “ CeO_2 ”. For the preparation of Al- or Ta-doped CeO_2 , cerium (III) nitrate hexahydrate and aluminum (III) chloride, or tantalic (V) chloride (the molar ratio of Al/Ce = 0.1, or Ta/Ce = 0.1) was simultaneously dissolved in the deionized water. The “Al-Ce” and “Ta-Ce” catalysts were obtained via the same process. Finally, the catalysts were sieved to 40 – 60 mesh for catalytic performance evaluation.

2.2. Catalytic performance evaluation

$\text{NH}_3\text{-SCR}$ of NO and CBCO activities of the prepared catalysts were performed in a fixed-bed quartz tube reactor. The temperature in the center of the reactor was measured by the thermocouple. The total flow rate was 200 ml min⁻¹. The typical reactant for the synergistic removal of NO/CB consisted of 500 ppm NH_3 , 500 ppm NO, 500 ppm CB, 10% O_2 , 5% H_2O , and N_2 balance gas. The corresponding gas hourly space velocity (GHSV) was 40,000 h⁻¹, and the range of reaction temperature was from 90 °C to 400 °C with a step of 30 °C. The concentrations of NO, NO_2 , CO, and CO_2 at the inlet and outlet were detected by flue gas analyzer, while CB and by-products were detected by gas chromatography (GC) equipped with FID. The SCR activity, CBCO activity, and synergistic removal activity of NO/CB over the catalyst were tested,

respectively.

The NO conversion, N_2 selectivity, CB conversion, and CO_2 selectivity were calculated regarding the following equation:

$$\text{NO}_x \text{ conversion} (\%) = 100\% \times \frac{[\text{NO}_x]_{in} - [\text{NO}_x]_{out}}{[\text{NO}_x]_{in}}$$

$$[\text{NO}_x] = [\text{NO}] + [\text{NO}_2]$$

$$\text{N}_2 \text{ selectivity} (\%) = 100\% \left(1 - \frac{2[\text{N}_2\text{O}]_{out}}{[\text{NO}_x]_{in} + [\text{NH}_3]_{in} - [\text{NO}_x]_{out} - [\text{NH}_3]_{out}} \right)$$

$$\text{CB conversion} (\%) = 100\% \frac{[\text{CB}]_{in} - [\text{CB}]_{out}}{[\text{CB}]_{in}}$$

$$\text{CO}_2 \text{ selectivity} (\%) = 100 \times \frac{[\text{CO}_2]_{out} - [\text{CO}_2]_{in}}{6 \times [\text{CB}]_{in}}$$

Where NO_x stood for the total concentration of NO and NO_2 , and “in” and “out” indicated the corresponding inlet and outlet gas concentrations, respectively.

2.3. Catalyst characterization

The powder XRD patterns were recorded on a Shimadzu XRD-7000 diffractometer using a Cu-K α radiation source (wavelength 1.5406 Å). An aluminum holder was used to support the catalyst simples. TEM, HRTEM, and EDS were conducted on a JEM-2100 microscope under the acceleration voltage of 200 kV. N_2 adsorption-desorption isotherm was measured on an Autosorb-iQ analyzer at 87 K. XPS was carried out on an ESCALAB 250XI. XRF analysis was carried out on a Shimadzu XRF-1800. $\text{NH}_3\text{-TPD}$ and $\text{H}_2\text{-TPR}$ were performed on the ChemBET Pulsar TPR/TPD. CB-TPD was performed in a quartz tube reactor system equipped with a Hiden HPR20 MS. Pyridine Infrared spectra of samples were recorded on the Nicolet Magna-IR 560. In situ DRIFTS were recorded using a Bruke VERTEX 70 spectrometers with KBr windows. Other experimental details were given in the [Supporting Information](#).

2.4. Computational methodology

The calculations were conducted using a linear combination of atomic orbitals (LCAO) DFT calculation employing the Dmol³ program in the materials studio 2017 package. The adsorption energy (E_{ad}), the formation energy of oxygen vacancy (ΔE_V) and differential charge density ($\Delta\rho$) were calculated by the following equation:

$$E_{ad} = E_{surf-iso} - (E_{surf} + E_{iso})$$

E_{surf} and E_{iso} are the energy of slab and an isolated atom or molecular respectively, while $E_{surf-iso}$ is the total energy. Note that the negative value for E_{ad} suggests a strong interaction between adsorption substrate and gas.

$$\Delta E_V = E_{O_{xv}} + \frac{1}{2}E_{O_2} - E_{O_x}$$

where O_x is the oxide (doped or not) and O_{xv} is the oxide with an oxygen vacancy on the surface.

$$\Delta\rho = \rho_{dopant/substrate} - \rho_{dopant} - \rho_{substrate}$$

$\rho_{dopant/substrate}$ was the charge density distribution of the system after Al or Ta doping on the slab model of catalyst, ρ_{dopant} and $\rho_{substrate}$ was the charge density distribution of the free dopant atom and substrate, respectively. For the doped oxides, the doped cation was not only on the surface but also in the bulk phase after crystallization. The coordination environment of the active site was dependent on the dopant cation on the surface of the catalyst, which directly affect the activity of the catalyst. The doping of cation on the surface of catalyst was the main

research object. The detail of calculation parameters, slab model description and transition state searching was given in the [Supporting Information](#).

3. Results and discussion

3.1. Structure of Al- and Ta-substituted CeO_2

As shown in [Fig. 1a](#) and b, the crystal structures of the Al-Ce, CeO_2 , and Ta-Ce catalysts were confirmed from X-ray powder diffraction (XRD) patterns to illustrate the effect of metal doping on the crystal structure. Al-Ce and Ta-Ce exhibited the same characteristic peak as CeO_2 without doping, all of the diffraction peaks were assigned to CeO_2 (PDF-43-1002), and no Al_2O_3 and Ta_2O_5 crystalline phases were found. Compared with CeO_2 , the peak position of (111) crystal face at around $2\theta = 28.5^\circ$ of Al-doped CeO_2 shifted to the left, due to that the Ce cation in the lattice substituted by the Al cation, whose radius was much smaller than that of Ce cation, caused the lattice spacing decreased [30]. Since the ionic radius of Ta and Ce was similar, there was no change in lattice parameters for Ta-doped CeO_2 . These results proved that a doped oxide had been well prepared.

High-resolution transmission electron microscopy (HRTEM) images were present to determine the substitution of Al or Ta into CeO_2 lattice. The image of CeO_2 showed the interplanar spacing of about 0.311 and 0.276 nm, corresponding to the (111) and (200) lattice fringes of the CeO_2 sample ([Fig. 1d](#)). The selected area electron diffraction (SAED) (inset of [Fig. 1d](#)) further confirmed the CeO_2 structure within the Fm-3 m (225) space group. Comparing the images of the CeO_2 and Al-Ce catalysts, it could be found that interplanar spacing of the same diffraction plane was different ([Fig. 1c](#)). Similarly, Ta-Ce showed the same result ([Fig. 1e](#)). These experimental results indicated that lattice Ce

atoms were partially substituted by Al or Ta. EDS elemental mapping images further demonstrated the presence of Al in Al-Ce and Ta in Ta-Ce, implying that the doping element might exist in anatomically dispersed state, and Al-Ce and Ta-Ce oxide solid solution was formed ([Fig. 1f](#) and g). The molar ratio of doped atom to Ce atom was about 8% in the Al-Ce, Ta-Ce catalyst ([Table S1](#)). The TEM images of Al-Ce, Ce, and Ta-Ce exhibited the same microscopic morphology with irregular polygonal sheet structure, and an average size of 10 nm ([Fig. S1](#)). Moreover, the three catalysts showed similar Brunauer-Emmett-Teller (BET) specific surface area and pore size distribution ([Fig. S2](#) and [Table S2](#)). The above experimental results showed that the three catalysts had similar physical properties and gas accessibility, which excluded other non-major factors for the subsequent studies on the types and properties of active sites, caused by the high and low valent substitution.

3.2. Catalytic performance for the removal of NO and/or CB

The effect of different valent substitutions on the activity of selective catalytic reduction of NO was examined in the temperature range of 100 – 400 °C ([Fig. 2a](#)). Under the reaction conditions of 500 ppm NH_3 , 500 ppm NO, 10% O_2 , 5% H_2O , and N_2 balance gas, the CeO_2 catalyst showed NO conversion of 76% and N_2 selectivity of 92% at 180 °C. When the Ce^{4+} cation of CeO_2 was substituted by low valent Al^{3+} , the NO conversion curve as a function of temperature slightly shifted to the left. The Al-Ce catalyst showed NO conversion of 87% and N_2 selectivity of 94% at 180 °C. When the Ce^{4+} ion of CeO_2 was substituted by high valent Ta^{5+} , the NO conversion curve showed an obvious right shift in the low-temperature region and had no obvious change at a temperature above 250 °C. The Ta-Ce catalyst showed the lowest NH_3 -SCR activity among the synthesized catalysts. A little NO_2 byproducts were detected over the present three catalysts below 200 °C in the SCR and SCR/CBCO

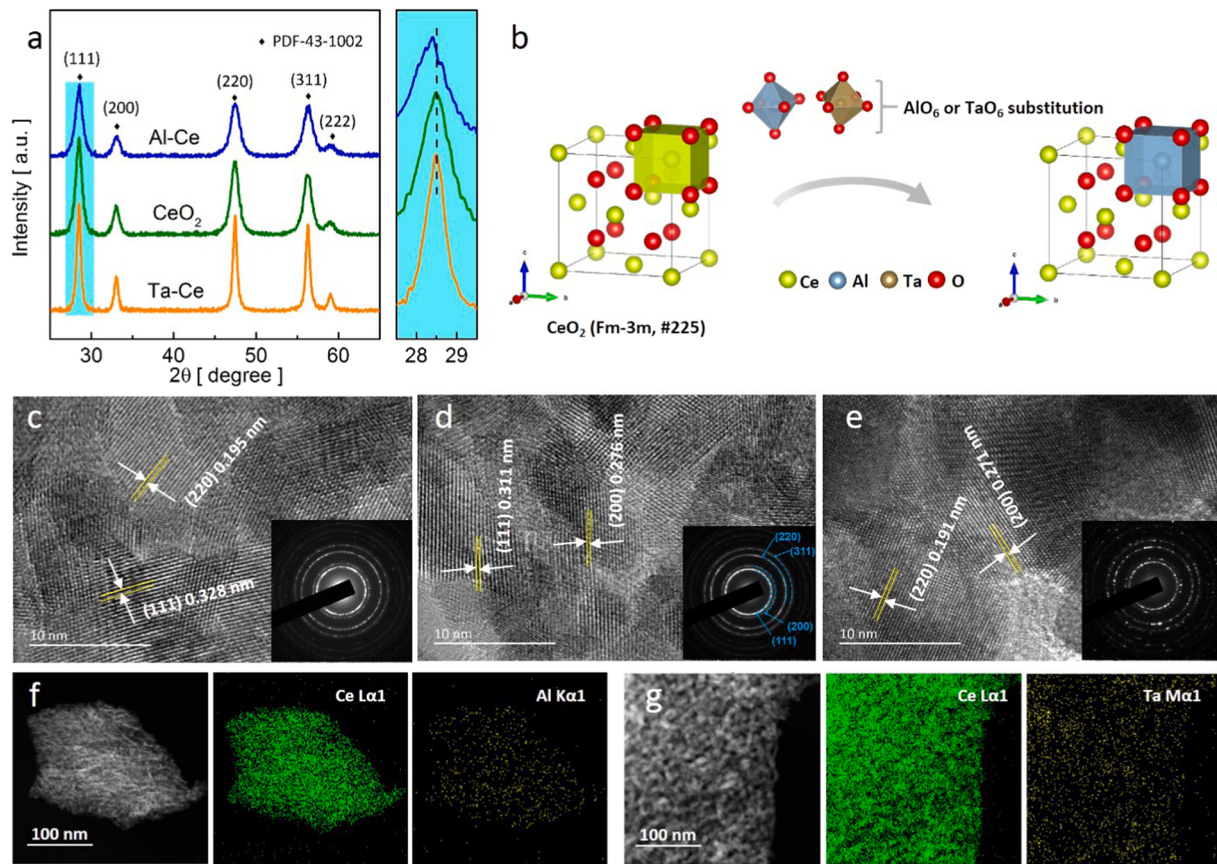


Fig. 1. (a) XRD patterns; (b) schematic illustration; and HRTEM images (inset: SAED) of (c) Al-Ce, (d) CeO_2 , and (e) Ta-Ce; elemental mapping of (f) Al-Ce and (g) Ta-Ce.

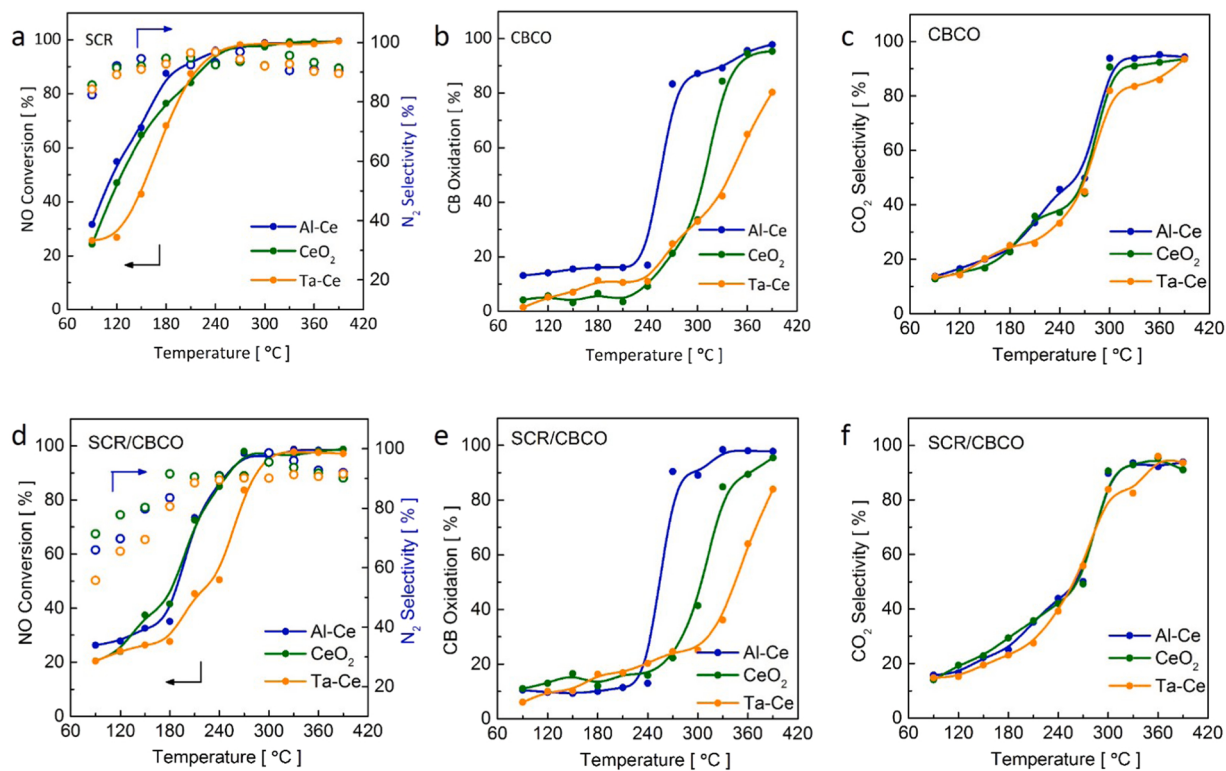


Fig. 2. (a) NO conversion and N₂ selectivity in the SCR; (b) CB conversion and (c) CO₂ selectivity in the CBCO; (d) NO conversion and N₂ selectivity in the SCR/CBCO; (e) CB conversion and (f) CO₂ selectivity in the SCR/CBCO.

reaction. It's worth noting that the Al-Ce catalyst favored the NO oxidation into NO₂ that subsequently enhanced the fast SCR routine (Fig. S3). These results indicated that substituting with different valent metal cations could affect the catalytic activity, and the incorporation of lower valent ions (Al³⁺) into CeO₂ exhibited better activity. Under the reaction conditions of 500 ppm CB, 10% O₂, 5% H₂O, and N₂ balance gas, the catalytic oxidation of CB was examined over the Al-Ce, CeO₂, and Ta-Ce catalysts (Fig. 2b and c). All three catalysts showed a low CB oxidation rate and CO₂ selectivity at a temperature below 250 °C. The CB conversion over the Al-Ce catalyst was much higher than that over the CeO₂ catalyst above 250 °C, while the CB conversion over the Ta-Ce catalyst was lower than that over the CeO₂ catalyst. The temperature required for 80% conversion (T_{80}) of CB was 274 °C, 335 °C, and 390 °C over the Al-Ce, CeO₂, and Ta-Ce catalysts, respectively. The CO₂ selectivity increased with a rise in the temperature. Thus, for the catalytic oxidation of CB, the catalytic activity of CeO₂ was significantly increased by the substitution of low valent Al³⁺, while it was significantly inhibited by the substitution of high valent Ta⁵⁺.

Under the reaction conditions of 500 ppm NH₃, 500 ppm NO, 500 ppm CB, 10% O₂, 5% H₂O, and N₂ balance gas, the NO conversion at 180 °C was 35%, 41%, and 27% over the Al-Ce, CeO₂, and Ta-Ce catalysts, respectively. It was further indicated that compared with CeO₂, the substitution of high valent Ta⁵⁺ decreased the catalytic activity, and Al³⁺-doped CeO₂ showed similar NH₃-SCR activity (Fig. 2d). Over the Al-Ce catalyst, when CB was introduced to the reaction gas, NO conversion and N₂ selectivity at 180 °C were drastically decreased from 87% to 35%, and 94–82%, respectively. Over the CeO₂ and Ta-Ce catalysts, the conversion of NO in the synergistic removal of NO/CB was also decreased compared with that in the NH₃-SCR of NO. It should be noted that at a high reaction temperature (> 300 °C), the inhibitory effect of CB on the NO conversion and N₂ selectivity was not obvious, for the synergistic removal of NO/CB. The decrease in the NH₃-SCR of NO activity in the presence of CB might be caused by the competitive adsorption between NH₃ and CB on the same active sites, or the

inhibition of the catalytic cycle by undecomposed CB at low temperature such as 180 °C [31]. The N₂ selectivity decreased slowly when the temperature exceeded 240 °C for both SCR and SCR/CBCO, which might be due to the increase of N₂O and other by-products caused by direct oxidation of ammonia. Shown in Fig. 2e and f were the CB conversion and CO₂ selectivity as a function of reaction temperature for the synergistic removal of NO/CB. It could be seen that the CB conversion and CO₂ selectivity were significantly increased, when the reaction temperature was above 240 °C. Interestingly, the corresponding T_{80} of CB over the Al-Ce, CeO₂, and Ta-Ce catalysts were 274 °C, 335 °C, and 387 °C. The different valent states of doped cations affected the type and amount of active sites of the catalyst. Over the present catalysts, the variation trend of CB conversion and CO₂ selectivity in the synergistic removal of NO/CB kept consistent with that for the catalytic oxidation of CB. In other words, the presence of NH₃ and NO had little effect on the oxidation of CB. Moreover, the Al-Ce catalyst exhibited high catalytic stability (Fig. S4), and the conversion of NO and CB at 270 °C did not exhibit an obvious decrease within 30-h on stream reaction.

3.3. Redox ability and acidity analysis

X-ray photoelectron spectroscopy (XPS) analysis was performed to obtain the composition information. The Ce 3d XPS spectra could be deconvoluted into ten components (Fig. 3a). Specifically, the peaks v₀, v, v', v'', and v''' were attributed to the 3d_{5/2} orbital of Ce cation, and the peaks of u₀, u, u', u'', and u''' were assigned to the 3d_{3/2} orbital of Ce cation. Among the components, the spin-orbit split doublets including v, v', v'', u, u', and u''' was corresponded to Ce⁴⁺, and the other four peaks indicated the presence of Ce³⁺ [32]. The molar ratio of Ce³⁺/(Ce⁴⁺ + Ce³⁺) of the Al-Ce catalyst was lower than that of the CeO₂ catalyst, while that of the Ta-Ce catalyst was higher than that of CeO₂ catalyst (Fig. 3c). It is understandable for the surface charge balance. In the Al-Ce and Ta-Ce catalysts, partial Ce⁴⁺ was substituted by Al³⁺ and Ta⁵⁺, respectively. The peak at 73.7 eV for the Al-Ce catalyst

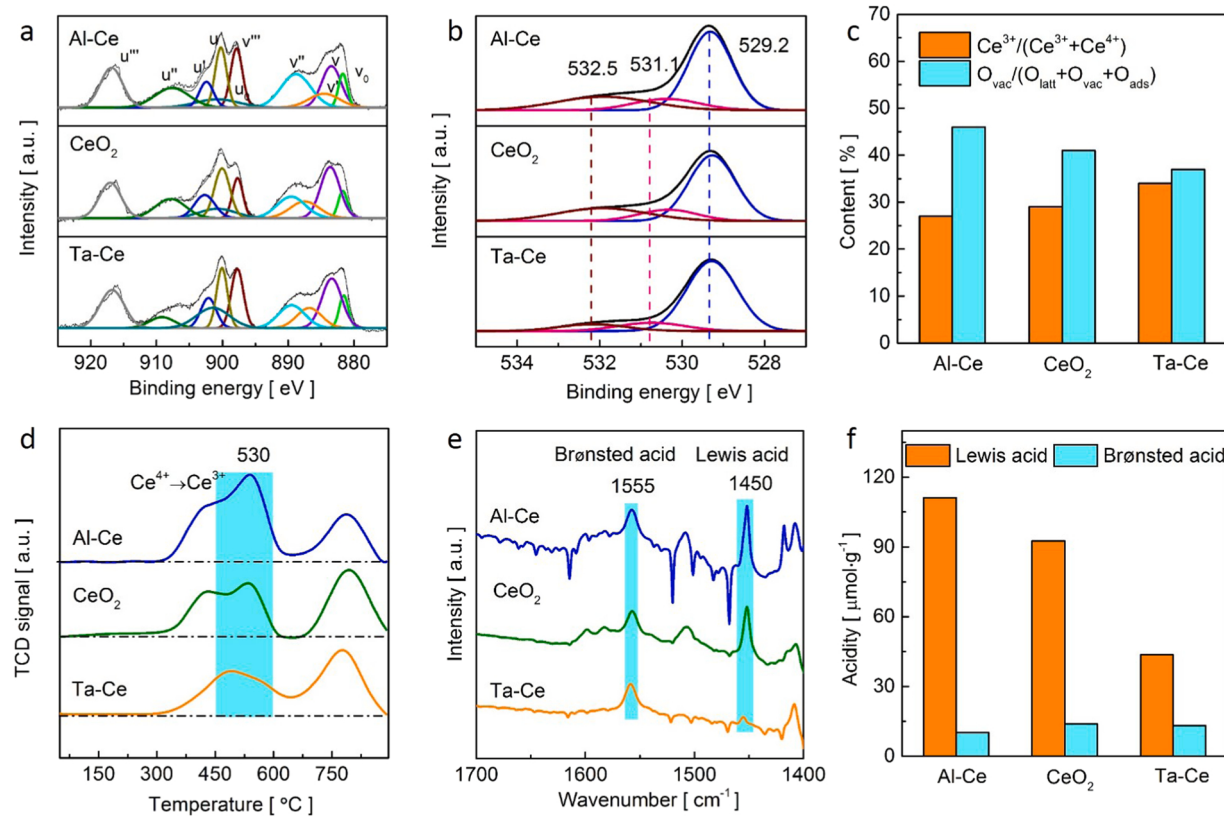


Fig. 3. XPS spectra of (a) Ce 3d and (b) O 2p; (c) $\text{Ce}^{3+}/(\text{Ce}^{3+} + \text{Ce}^{4+})$ and $\text{O}_{\text{vac}}/(\text{O}_{\text{latt}} + \text{O}_{\text{vac}} + \text{O}_{\text{ads}})$ molar ratio obtained by XPS peak deconvolution; (d) TPR spectra; (e) Pyridine-IR spectra; (f) acidity amount obtained by Pyridine-IR.

was assigned to the Al 2p orbital of Al^{3+} (Fig. S5). There were two peaks at binding energies of 25.7 and 27.7 eV for the Ta-Ce catalyst, which was respectively attributed to the Ta 4 $f_{7/2}$ and Ta 4 $f_{5/2}$ orbitals of Ta^{5+} . These results revealed that Al^{3+} and Ta^{5+} preferentially replaced Ce^{4+} on the octahedral position of CeO_2 .

The O 1 s XPS spectra of the present catalysts could be fitted into three components. The peaks at binding energies of 529.0, 529.6, and 531.7 eV were ascribed to the lattice oxygen (O_{latt}), oxygen vacancies (O_{vac}), and chemisorbed oxygen species (O_{ads} , e.g. O_2^- and O_2^{2-}), respectively (Fig. 3b) [33,34]. The ratio of $\text{O}_{\text{vac}}/(\text{O}_{\text{latt}} + \text{O}_{\text{vac}} + \text{O}_{\text{ads}})$ in the Ta-Ce catalyst was the lowest among the three catalysts, which indicated that the formation of O_{vac} was suppressed by the incorporation of Ta^{5+} into CeO_2 (Fig. 3c). This was due to that the higher valent Ta^{5+} contributed more electrons than that of substituted Ce^{4+} , resulting in the amount of O_{ads} increased, while O_{latt} that gained more electrons was not easy to escape from the surface of the catalyst.

The reducibility of catalysts had been evaluated by H_2 -TPR (Fig. 3d). The peaks at around 530 °C corresponded to the reduction of surface Ce^{4+} [32,35]. For the Al-Ce catalyst, the H_2 consumption in the region of 300–600 °C was higher than that of the CeO_2 catalyst, indicating that the substitution of Al^{3+} promoted the reducibility of the catalyst. On the contrary, the doping of Ta^{5+} inhibited the reduction of Ce^{4+} on the surface of the catalyst. The Ta^{5+} cation in the Ta-Ce catalyst was more easily reduced by hydrogen, which resulted in the TPR profile of the Ta-Ce catalyst moving to a lower temperature compared with the Al-Ce and CeO_2 samples. These results were consistent with the results of the XPS analysis above. Pyridine IR analysis was carried out to study the influence of doped cations on the active site of CeO_2 . The bands at 1450 and 1555 cm^{-1} were attributed to the adsorption of pyridine vapor at Lewis acidic sites and Brønsted acidic sites respectively (Fig. 3e) [36]. All the samples exhibited abundant Lewis acidities and slight Brønsted acidities. Compared to the CeO_2 catalyst, the Lewis acidic sites in the

Al-Ce catalyst increased to 111.2 $\mu\text{mol}/\text{g}$, and the change in the amount of Brønsted acid sites was negligible, which indicated that the incorporation of lower valent cations Al^{3+} into CeO_2 could promote the formation of Lewis acid on the catalyst surface (Fig. 3f). This was due to that Al^{3+} in the lattice contributed fewer electrons than Ce^{4+} , and it could receive extra electrons. Conversely, Ta^{5+} was an electron donor due to that it contributed more electrons than Ce^{4+} , resulting in the Lewis acidic sites in Ta-Ce catalyst decreasing to 43.6 $\mu\text{mol}/\text{g}$. Combined with the catalytic activity tests, it could be seen that the number of Lewis acid sites could be controlled by doped cations, and the activity of NH_3 -SCR was positively correlated with the quantity of Lewis acid sites.

3.4. Adsorption of reaction gases

The above studies focused on the regulation mechanism of different valent doping on the active sites of the catalysts. The interaction between the active sites of different catalysts and the reactant molecules was studied in depth. In situ diffuse reflectance infrared Fourier transform (DRIFT) measurements under different conditions were conducted to identify the adsorption process and intermediate states of reactant molecules. At present, Langmuir-Hinshelwood and Eley-Rideal mechanism were generally accepted for the NH_3 -SCR reaction mechanism, both of which emphasized the adsorption of NH_3 as the first step of the reaction [37]. Thus, we used NH_3 as a probe molecule to study the nature of active sites for all the synthesized catalysts. As shown in Fig. 4a, after the catalyst was exposed to 500 ppm NH_3 for 10 min, the bands at 1250 and 1410 cm^{-1} were attributed to the symmetric vibrations of the N-H of NH_3 coordinated to Lewis acid sites and the asymmetric vibration of NH_4^+ species coordinated to Brønsted acid sites, respectively [25]. The peak area corresponded to the Lewis acid sites of Al-Ce catalyst was larger than that of CeO_2 , which indicated that incorporation of Al^{3+} could increase the number of Lewis acid sites and promote NH_3

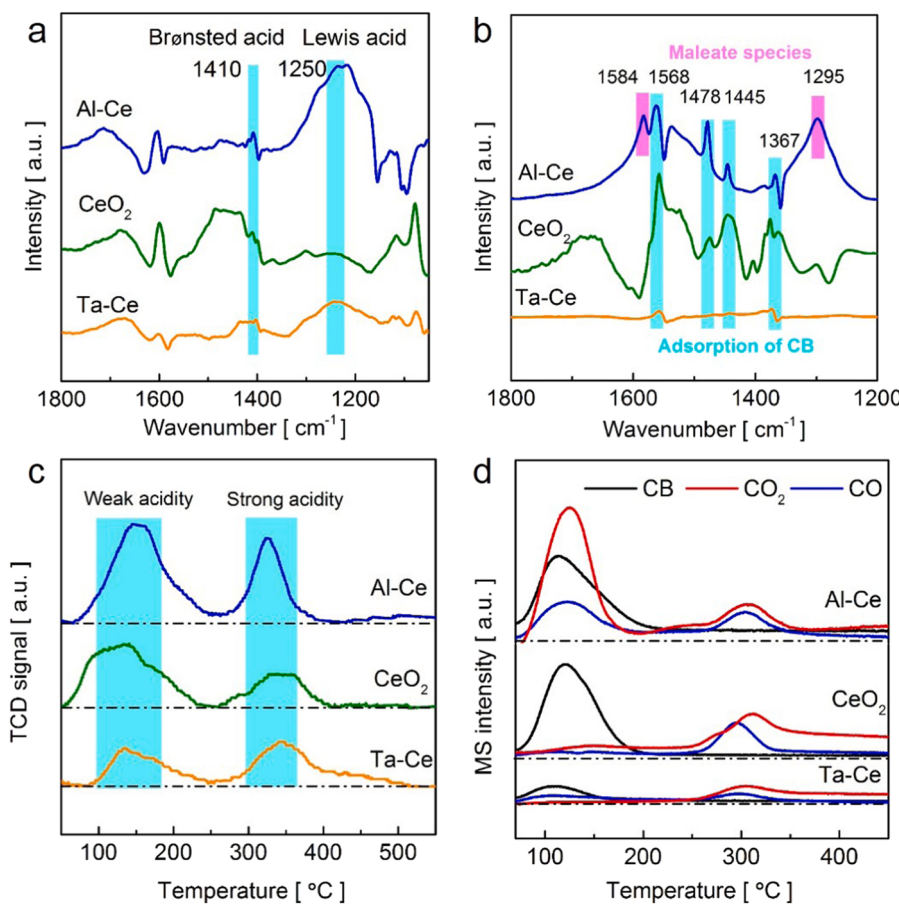


Fig. 4. in situ DRIFT spectra of (a) NH₃ adsorption and (b) CB adsorption; (c) NH₃-TPD curves; (d) CB-TPD-MS curves.

adsorption, which was the main reason for the better NH₃-SCR activity of Al-Ce catalyst. The adsorption of NH₃ at Lewis acid sites of Ta-Ce catalyst was the lowest among all the present catalysts, which further verified the inhibition of SCR activity by high valent cation doping. These results were consistent with Pyridine-IR analysis. As shown in Fig. 4b, after the catalyst was exposed to 500 ppm CB for 10 min, the bands at 1445, 1478, and 1568 cm⁻¹ were assigned to aromatic C=C vibration, and the bands at 1367 cm⁻¹ corresponded to carbonate bidentate [38,39]. For the Al-Ce catalyst, in addition to the characteristic peak of CB found in CeO₂, the band at 1295 and 1584 cm⁻¹ attributed to carboxylate were also detected, which indicated that the lattice oxygen of Al-Ce has a strong oxidation ability leading to the ring-opening reaction of CB [40–43]. For the Ta-Ce, only the characteristic peak of CB was found and the strength was much lower than that of Al-Ce and CeO₂ catalyst. The incorporation of higher valent cations Ta⁵⁺ into CeO₂ made the lattice oxygen acquire more electrons, which weakened its oxidation capacity and hindered the oxidation of CB.

All the catalysts exhibited two broad NH₃ desorption peaks, located at the temperature range of 100–250 °C and 270–400 °C, corresponding to the weak acidity and strong acidity, respectively (Fig. 4c) [44,45]. Comparing the desorption amount of NH₃, it could be seen that low and high valent doping have positive and negative effects on the adsorption of NH₃, respectively (Fig. S6). These results were consistent with the above in situ DRIFT spectra of NH₃ adsorption. CB-TPD/MS experiments were employed to investigate the desorption process of CB on the catalyst surface and related products (Fig. 4d). For the Al-Ce catalyst, the CB desorption peaks at 120 °C were assigned to the CB weak chemisorption on the surface of the catalyst. The desorption peak of CO and CO₂ at 120 °C was corresponded to intermediate during the oxidation of CB, while the desorption peak at 310 °C was due to the

decomposition of organic fragments on the surface of the catalyst [46]. The oxygen ion coordinated with Al³⁺ has a stronger oxidation capacity, so the incomplete oxidation decomposition reaction of CB at 120 °C could occur, which was consistent with the results of the activity test that showed about 20% conversion at 120 °C. For the CeO₂ catalyst, the desorption peak of CO and CO₂ at 120 °C was not found, and the desorption peak area of CB was much larger than that of Al-Ce, which indicated that the adsorption strength of CB on CeO₂ was weak and a small decomposition reaction occurred. For the Ta-Ce catalyst, the desorption peak area of CB, CO, and CO₂ was the smallest among all synthesized catalysts. This was due to the doping of high valent Ta⁵⁺ donating more electrons to the coordination oxygen, leading to the decrease of oxidizability of coordination oxygen, thus reducing the oxidation decomposition of chemisorbed CB. Organic chlorinated products (C₂H₂Cl₂) and inorganic chlorine compounds (HCl and Cl₂) were detected at various temperatures. The H₂O molecule generated from the NH₃-SCR reaction promoted the formation of HCl as a hydrogen donor, and improved the chlorine tolerance of catalysts (Fig. S7).

3.5. Reaction energy and electron analysis

Density functional theory (DFT) calculations were carried out to get more insights on how the properties of the active site were affected by doping cations. For comparison, the Al-Ce, Ta-Ce, and bulk CeO₂(111) surface structures were examined (Fig. S8). The adsorption energy of NH₃ (adsorbed on the top of cation) on different catalysts was compared, and the Al-Ce catalyst with an E_{ads} of −0.73 eV was thermodynamically favorable compared with the CeO₂ (−0.41 eV) and Ta-Ce (−0.01 eV) catalysts (Fig. 5). This indicated that the doping of Al³⁺ into CeO₂ could

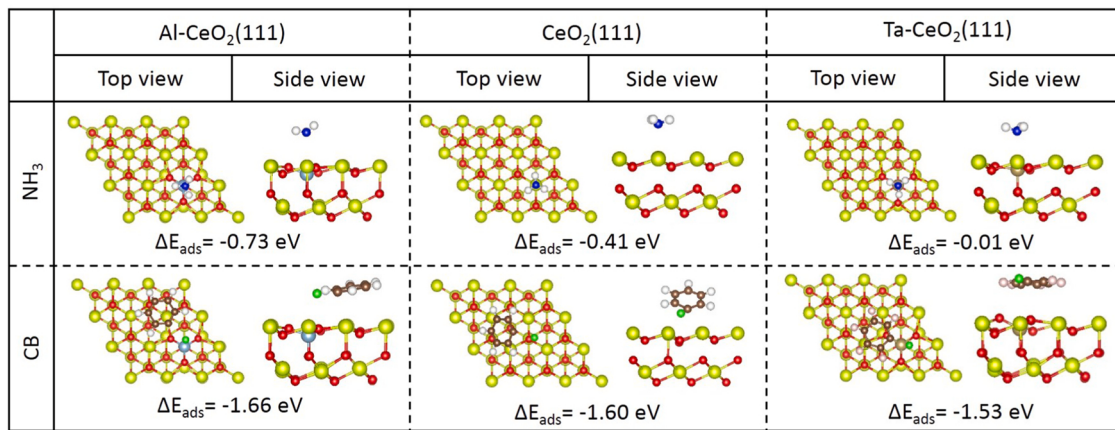


Fig. 5. The optimized structure and energy of NH₃ or CB adsorbed on the Al-Ce, CeO₂, and Ta-Ce structure. Atom color: blue: N, white: H, green: Cl, gray: C. (For interpretation of the references to colour in this figure, the reader is referred to the web version of this article.)

form stronger Lewis acid sites to capture the free NH₃ molecules, confirming the observed better SCR activity of the Al-Ce catalyst. There was no significant difference in the three catalysts for the adsorption energy of CB, which might be due to the CB adsorbed on the catalyst surface in a parallel manner and bonded with multiple oxygen sites and cation sites (Fig. 5).

The NH₃-SCR activity could be reflected by the activation energy of the first N-H scission of NH₃, where a better catalyst should present a ΔE_{N-H} value close to zero [47]. The calculated N-H activation of NH₃ for the Al-Ce, CeO₂, Ta-Ce structures were 0.37, 0.79, and 1.03 eV, respectively (Fig. 6a, and Fig. S9). The lowest ΔE_{N-H} value of the Al-Ce catalyst suggested that the incorporation of Al³⁺ could effectively weaken the strength of N-H. The CB was oxidized by the oxygen site on the catalyst surface layer following the MvK mechanism. The reoxidation of the surface was very fast in general, and therefore the

oxidation of CB with the surface oxygen was the rate-limiting step [48]. The ability of surface oxygen to act as an oxidizing agent was evaluated by examining the formation energy required for oxygen vacancy, where the better oxidant should have smaller ΔE_v [49,50]. The energy ΔE_v required for forming an oxygen vacancy for the Al-Ce, CeO₂, Ta-Ce structure were 1.95, 2.21, and 2.92 eV respectively, suggesting that the oxygen atom coordinated with Al³⁺ was more likely to escape from the surface of the catalyst, so it had stronger oxidation properties (Fig. 6b, and Fig. S10).

The differential charge density ($\Delta\rho$) and density of states (DOS) were calculated to further elucidate the tailoring of electronic structure by doping in an atom level [51]. The plane of the three O atoms coordinated to the Ce or doped atom on the top layer was created to visualize the differential charge density (Fig. 6c). Obvious electronic perturbations could be found for the Al-Ce structure in comparison with CeO₂, as

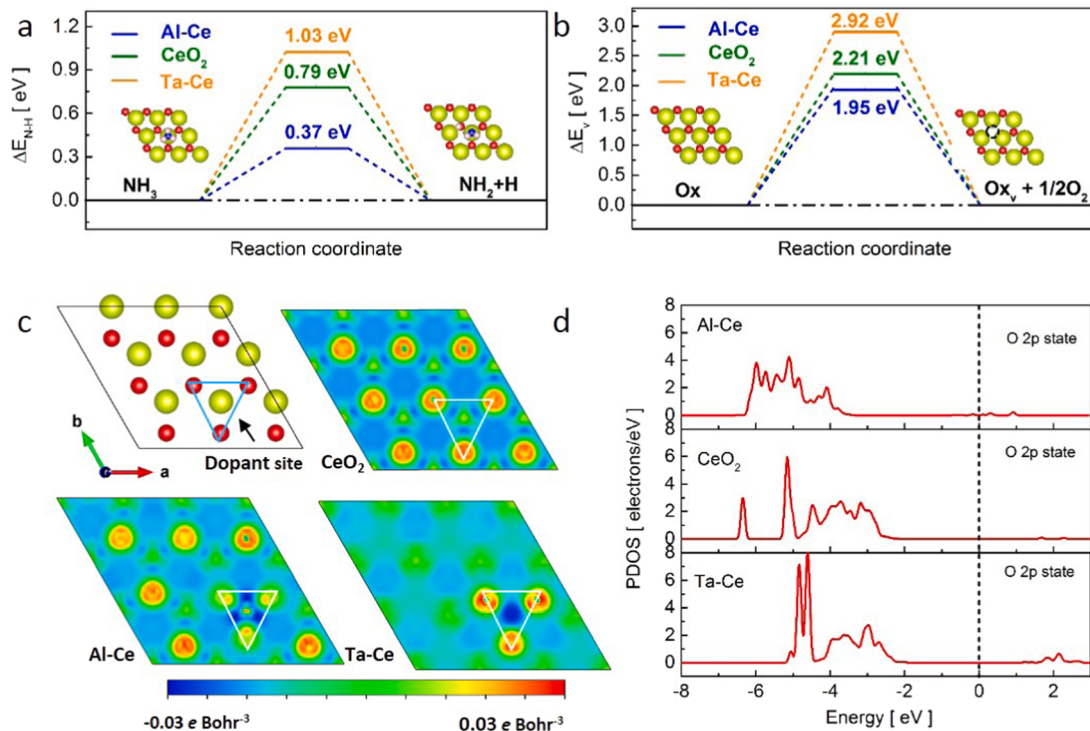


Fig. 6. (a) Calculated activation energy of the first N-H scission of NH₃ at the equilibrium potential; (b) calculated formation energy of oxygen vacancy at equilibrium potential; (c) differential charge density of CeO₂ after doping; (d) PDOS of O 2p for the Al-Ce, CeO₂, and Ta-Ce structure. Atom colors: yellow-Ce, red-O. (For interpretation of the references to colour in this figure, the reader is referred to the web version of this article.)

reflected by the change of electron density of oxygen coordinated with Al was less than that of O coordinated with Ce, which could be attributed to the smaller ionization energy of the Ce atom (534.4 kJ/mol) than that of the Al atom (577.5 kJ/mol). For the Ta-Ce structure, the degree of change in the electron density of O and Ta atoms was the highest among all samples, indicating that more electrons were transferred from Ta to O atom, thus leading to the higher oxygen vacancy formation energy of the Ta-Ce structure. Comparing the contribution of the O atom to the valence band, the position of O 2p states in the Al-Ce structure were at lower energy and faraway to the Fermi level than that of the CeO₂ and Ta-Ce structure, suggesting the stronger ability to accept electrons for the 2p orbital of O atom, which could facilitate the oxidation of CB with the surface oxygen (Fig. 6d). Therefore, lattice oxygen coordinated with Al³⁺ showed superior oxidation capacity, and promoted the formation of oxygen vacancy and dehydrogenation of NH₃, which was beneficial for the NH₃-SCR and CBCO reaction.

4. Conclusion

Generally, we systematically studied the electronic structure tailoring of CeO₂ by doping with different valent cations, as well as their activities in the synergistic degradation of NO/CB. HRTEM, EDS, and XRD characterization verified that the substitution of Al³⁺ or Ta⁵⁺ in CeO₂ lattice and homogeneously doped oxide had been well prepared. The Al-Ce catalyst exhibited remarkably improved NH₃-SCR of NO and CBCO activity in comparison with the CeO₂, whereas the Ta-Ce counterpart showed an opposite trend. Combining the XPS, TPD/MS, pyridine-IR, and in situ DRIFT investigations, the incorporation of Al³⁺ into CeO₂ formed a new Lewis acid site enhancing the adsorption of NH₃, which greatly contributed to SCR activity. Meanwhile, the Al³⁺ donated fewer electrons to the coordination oxygen than host cations resulting in the stability of dopant-oxide pairs being lower than that of the host-oxide pair, which was beneficial to the formation of oxygen vacancies and CB catalytic oxidation. On the contrary, high valent Ta⁵⁺ doping formed base sites and inhibited lattice oxygen separating from the surface of the catalyst, thus showing poor catalytic reduction and catalytic oxidation activities. Theoretical simulations further confirmed the activity of Al-Ce catalyst toward NH₃-SCR/CBCO with a low N-H scission and formation of oxygen vacancy barrier. Combined with the experimental and theoretical calculation results, it was found that the Lewis sites (low valent dopant/host cation site) and lattice oxygen sites were dominant for the SCR and CBCO reaction, respectively. The dopant-oxide pairs in the Al-Ce structure significantly tailored the electronic structure of O 2p states, which not only facilitated the N-H scission but also promoted the ability of surface oxygen to act as an oxidizing agent, thus leading to the better performance for the synergistic degradation of NO/CB. This work revealed the influence of doping on the properties of active sites, shedding light on designing efficient metal oxide catalysts with both catalytic reduction and catalytic oxidation capabilities.

CRediT authorship contribution statement

Lu Wei carried out experiments, wrote and modified the manuscript. Yuxi Liu, Hongxing Dai, Suping Cui, Can Wang, Hsing-Cheng Hsi, Erhong Duan, and Yue Peng analyzed the experimental results and modified the manuscript. Jiguang Deng designed the experiments, analyzed the experimental results, wrote and modified the manuscript.

Declaration of Competing Interest

The authors declare that they have no known competing financial interests or personal relationships that could have appeared to influence the work reported in this paper.

Acknowledgments

This work was supported by the China Postdoctoral Science Foundation (2020M680278), Natural Science Foundation of China (21961160743 and 21622701), National Key Research and Development Program of China (2016YFC0204800), and Natural Science Foundation of Hebei Province Key Project (B2021208033).

Appendix A. Supporting information

Supplementary data associated with this article can be found in the online version at doi:10.1016/j.apcatb.2021.120939.

References

- [1] W. Jiang, Y. Yu, F. Bi, P. Sun, X. Weng, Z. Wu, Synergistic elimination of NO_x and chloroaromatics on a commercial V₂O₅-WO₃/TiO₂ catalyst: Byproduct analyses and the SO₂ effect, Environ. Sci. Technol. 53 (2019) 12657–12667.
- [2] Y. Long, Y. Su, Y. Xue, Z. Wu, X. Weng, V₂O₅-WO₃/TiO₂ catalyst for efficient synergistic control of NO_x and chlorinated organics: insights into the arsenic effect, Environ. Sci. Technol. 55 (2021) 9317–9325.
- [3] G. He, M. Gao, Y. Peng, Y. Yu, W. Shan, H. He, Superior oxidative dehydrogenation performance toward NH₃ determines the excellent Low-Temperature NH₃-SCR activity of Mn-Based catalysts, Environ. Sci. Technol. 55 (2021) 6995–7003.
- [4] D. Wang, Q. Chen, X. Zhang, C. Gao, B. Wang, X. Huang, Y. Peng, J. Li, C. Liu, J. Crittenden, Multipollutant control (MPC) of flue gas from stationary sources using SCR technology: a critical review, Environ. Sci. Technol. 55 (2021) 2743–2766.
- [5] W. Tan, A. Liu, S. Xie, Y. Yan, T.E. Shaw, Y. Pu, K. Guo, L. Li, S. Yu, F. Gao, F. Liu, L. Dong, Ce-Si mixed oxide: a high sulfur resistant catalyst in the NH₃-SCR reaction through the mechanism-enhanced process, Environ. Sci. Technol. 55 (2021) 4017–4026.
- [6] Y. Li, S. Cai, P. Wang, T. Yan, J. Zhang, D. Zhang, Improved NO_x reduction over phosphate-modified Fe₂O₃/TiO₂ catalysts via tailoring reaction paths by in situ creating alkali-poisoning sites, Environ. Sci. Technol. 55 (2021) 9276–9284.
- [7] G. Li, K. Shen, L. Wang, Y. Zhang, H. Yang, P. Wu, B. Wang, S. Zhang, Synergistic degradation mechanism of chlorobenzene and NO_x over the multi-active center catalyst: The role of NO₂, Brønsted acidic site, oxygen vacancy, Appl. Catal. B 286 (2021), 119865.
- [8] L. Ye, P. Lu, X. Chen, P. Fang, Y. Peng, J. Li, H. Huang, The deactivation mechanism of toluene on Mn_x-CeO₂ SCR catalyst, Appl. Catal. B 277 (2020), 119257.
- [9] Y. Huo, K. Liu, J. Liu, H. He, Effects of SO₂ on standard and fast SCR over CeWO_x: a quantitative study of the reaction pathway and active sites, Appl. Catal. B 301 (2022), 120784.
- [10] W. Deng, Q. Tang, S. Huang, L. Zhang, Z. Jia, L. Guo, Low temperature catalytic combustion of chlorobenzene over cobalt based mixed oxides derived from layered double hydroxides, Appl. Catal. B 278 (2020), 119336.
- [11] X. Hu, J. Chen, W. Qu, R. Liu, D. Xu, Z. Ma, X. Tang, Sulfur-resistant ceria-based low-temperature SCR catalysts with the non-bulk electronic states of ceria, Environ. Sci. Technol. 55 (2021) 5435–5441.
- [12] C. Croisé, R. Pointecouteau, J. Akil, A. Demourges, N. Bion, X. Courtois, F. Can, Insight into the praseodymium effect on the NH₃-SCR reaction pathways over W or Nb supported ceria-zirconia based catalysts, Appl. Catal. B 298 (2021), 120563.
- [13] N. Zhu, Y. Shan, W. Shan, Y. Sun, K. Liu, Y. Zhang, H. He, Distinct NO₂ effects on Cu-SSZ-13 and Cu-SSZ-39 in the selective catalytic reduction of NO_x with NH₃, Environ. Sci. Technol. 54 (2020) 15499–15506.
- [14] L. Kang, L. Han, P. Wang, C. Feng, J. Zhang, T. Yan, J. Deng, L. Shi, D. Zhang, SO₂-Tolerant NO_x reduction by marvelously suppressing SO₂ adsorption over Fe₃Ce_{1-x}VO₄ catalysts, Environ. Sci. Technol. 54 (2020) 14066–14075.
- [15] X. Weng, Y. Xue, J. Chen, Q. Meng, Z. Wu, Elimination of chloroaromatic congeners on a commercial V₂O₅-WO₃/TiO₂ catalyst: the effect of heavy metal Pb, J. Hazard. Mater. 387 (2020), 121705.
- [16] Q. Dai, K. Shen, W. Deng, Y. Cai, J. Yan, J. Wu, L. Guo, R. Liu, X. Wang, W. Zhan, HCl-Tolerant H_xPO₄/RuO_x-CeO₂ catalysts for extremely efficient catalytic elimination of chlorinated VOCs, Environ. Sci. Technol. 55 (2021) 4007–4016.
- [17] X. Weng, Q. Meng, J. Liu, W. Jiang, S. Pattisson, Z. Wu, Catalytic oxidation of chlorinated organics over lanthanide perovskites: Effects of phosphoric acid etching and water vapor on chlorine desorption behavior, Environ. Sci. Technol. 53 (2019) 884–893.
- [18] D. Wang, J. Chen, Y. Peng, W. Si, X. Li, B. Li, J. Li, Dechlorination of chlorobenzene on vanadium-based catalysts for low-temperature SCR, Chem. Commun. 54 (2018) 2032–2035.
- [19] L. Gan, W. Shi, K. Li, J. Chen, Y. Peng, J. Li, Synergistic promotion effect between NO_x and chlorobenzene removal on Mn_x-CeO₂ catalyst, ACS Appl. Mater. Interfaces 10 (2018) 30426–30432.
- [20] J.A. Martín-Martín, M. Gallastegi-Villa, M.P. González-Marcos, A. Aranzabal, J. R. González-Velasco, Bimodal effect of water on V₂O₅/TiO₂ catalysts with different vanadium species in the simultaneous NO reduction and 1,2-dichlorobenzene oxidation, Chem. Eng. J. 417 (2021), 129013.
- [21] X. Feng, M. Tian, C. He, L. Li, J. Shi, Y. Yu, J. Cheng, Yolk-shell-like mesoporous CoCr_x with superior activity and chlorine resistance in dichloromethane destruction, Appl. Catal. B 264 (2020), 118493.

[22] Y. Shi, Z. Li, J. Wang, R. Zhou, Synergistic effect of Pt/Ce and USY zeolite in Pt-based catalysts with high activity for VOCs degradation, *Appl. Catal. B* 286 (2021), 119936.

[23] E.W. McFarland, H. Metiu, Catalysis by doped oxides, *Chem. Rev.* 113 (2013) 4391–4427.

[24] Q. Huang, Z. Meng, R. Zhou, The effect of synergy between Cr_2O_3 - CeO_2 and USY zeolite on the catalytic performance and durability of chromium and cerium modified USY catalysts for decomposition of chlorinated volatile organic compounds, *Appl. Catal. B* 115–116 (2012) 179–189.

[25] Y. Inomata, H. Kubota, S. Hata, E. Kiyonaga, K. Morita, K. Yoshida, N. Sakaguchi, T. Toyao, K. Shimizu, S. Ishikawa, W. Ueda, M. Haruta, T. Murayama, Bulk tungsten-substituted vanadium oxide for low-temperature NO_x removal in the presence of water, *Nat. Commun.* 12 (2021) 557.

[26] Z. Liu, G. Sun, C. Chen, K. Sun, L. Zeng, L. Yang, Y. Chen, W. Wang, B. Liu, Y. Lu, Y. Pan, Y. Liu, C. Liu, Fe-doped Mn_3O_4 spinel nanoparticles with highly exposed $\text{Fe}_{\text{oct}}\text{-O-Mn}_{\text{tet}}$ sites for efficient selective catalytic reduction (SCR) of NO with ammonia at low temperatures, *ACS Catal.* 10 (2020) 6803–6809.

[27] L. Han, S. Cai, M. Gao, J. Hasegawa, P. Wang, J. Zhang, L. Shi, D. Zhang, Selective catalytic reduction of NO_x with NH_3 by using novel catalysts: state of the art and future prospects, *Chem. Rev.* 119 (2019) 10916–10976.

[28] H. Xu, J. Liu, Z. Zhang, S. Liu, Q. Lin, Y. Wang, S. Dai, Y. Chen, Design and synthesis of Highly-Dispersed WO_3 catalyst with highly effective NH_3 -SCR activity for NO_x abatement, *ACS Catal.* 9 (2019) 11557–11562.

[29] K. Mishra, T.N. Poudel, N. Basavegowda, Y.R. Lee, Enhanced catalytic performance of magnetic $\text{Fe}_2\text{O}_4\text{-MnO}_2$ nanocomposites for the decolorization of rhodamine B, reduction of 4-nitroaniline, and sp3C-H functionalization of 2-methylpyridines to isatins, *J. Catal.* 344 (2016) 273–285.

[30] P. Yang, S. Yang, Z. Shi, Z. Meng, R. Zhou, Deep oxidation of chlorinated VOCs over CeO_2 -based transition metal mixed oxide catalysts, *Appl. Catal. B* 162 (2015) 227–235.

[31] D. Zengel, M. Stehle, O. Deutschmann, M. Casapu, J. Grunwaldt, Impact of gas phase reactions and catalyst poisons on the NH_3 -SCR activity of a $\text{V}_2\text{O}_5\text{-WO}_3\text{/TiO}_2$ catalyst at pre-turbo position, *Appl. Catal. B* 288 (2021), 119991.

[32] Z. Su, W. Yang, C. Wang, S. Xiong, X. Cao, Y. Peng, W. Si, Y. Weng, M. Xue, J. Li, Roles of oxygen vacancies in the bulk and surface of CeO_2 for toluene catalytic combustion, *Environ. Sci. Technol.* 54 (2020) 12684–12692.

[33] H. Liu, X. Li, Q. Dai, H. Zhao, G. Chai, Y. Guo, Y. Guo, L. Wang, W. Zhan, Catalytic oxidation of chlorinated volatile organic compounds over Mn-Ti composite oxides catalysts: elucidating the influence of surface acidity, *Appl. Catal. B* 282 (2021), 119577.

[34] Z. Jiang, M. Jing, X. Feng, J. Xiong, C. He, M. Douthwaite, L. Zheng, W. Song, J. Liu, Z. Qu, Stabilizing platinum atoms on CeO_2 oxygen vacancies by metal-support interaction induced interface distortion: Mechanism and application, *Appl. Catal. B* 278 (2020), 119304.

[35] G. Ou, Y. Xu, B. Wen, R. Lin, B. Ge, Y. Tang, Y. Liang, C. Yang, K. Huang, D. Zu, R. Yu, W. Chen, J. Li, H. Wu, L. Liu, Y. Li, Tuning defects in oxides at room temperature by lithium reduction, *Nat. Commun.* 9 (2018) 1302.

[36] P. Sun, S. Zhai, J. Chen, J. Yuan, Z. Wu, X. Weng, Development of a multi-active center catalyst in mediating the catalytic destruction of chloroaromatic pollutants: A combined experimental and theoretical study, *Appl. Catal. B* 272 (2020), 119015.

[37] W. Qu, X. Liu, J. Chen, Y. Dong, X. Tang, Y. Chen, Single-atom catalysts reveal the dinuclear characteristic of active sites in NO selective reduction with NH_3 , *Nat. Commun.* 11 (2020) 1532.

[38] M. Nagao, Y. Suda, Adsorption of benzene, toluene, and chlorobenzene on titanium dioxide, *Langmuir* 5 (1989) 42–47.

[39] S. Krishnamoorthy, J.A. Rivas, M.D. Amiridis, Catalytic oxidation of 1,2-dichlorobenzene over supported transition metal oxides, *J. Catal.* 193 (2000) 264–272.

[40] S. Zhao, F. Hu, J. Li, Hierarchical core-shell $\text{Al}_2\text{O}_3\text{@Pd-CoAlO}$ microspheres for low-temperature toluene combustion, *ACS Catal.* 6 (2016) 3433–3441.

[41] K. Li, J. Chen, B. Bai, S. Zhao, F. Hu, J. Li, Bridging the reaction route of toluene total oxidation and the structure of ordered mesoporous Co_3O_4 : the roles of surface sodium and adsorbed oxygen, *Catal. Today* 297 (2017) 173–181.

[42] H. Huang, Y. Gu, J. Zhao, X. Wang, Catalytic combustion of chlorobenzene over $\text{VO}_x\text{/CeO}_2$ catalysts, *J. Catal.* 326 (2015) 54–68.

[43] L. Zhao, Z. Zhang, Y. Li, X. Leng, T. Zhang, F. Yuan, X. Niu, Y. Zhu, Synthesis of Ce_aMnO_x hollow microsphere with hierarchical structure and its excellent catalytic performance for toluene combustion, *Appl. Catal. B* 245 (2019) 502–512.

[44] X. Li, J. Li, Y. Peng, X. Li, K. Li, J. Hao, Comparison of the structures and mechanism of arsenic deactivation of $\text{CeO}_2\text{-MoO}_3$ and $\text{CeO}_2\text{-WO}_3$ SCR catalysts, *J. Phys. Chem. C* 120 (2016) 18005–18014.

[45] D.W. Kwon, D.H. Kim, S. Lee, J. Kim, H.P. Ha, A dual catalytic strategy by the nature of the functionalization effect as well as active species on vanadium-based catalyst for enhanced low temperature SCR, *Appl. Catal. B* 289 (2021), 120032.

[46] Q. Dai, J. Wu, W. Deng, J. Hu, Q. Wu, L. Guo, W. Sun, W. Zhan, X. Wang, Comparative studies of P/CeO_2 and Ru/CeO_2 catalysts for catalytic combustion of dichloromethane: from effects of H_2O to distribution of chlorinated by-products, *Appl. Catal. B* 249 (2019) 9–18.

[47] P. Kuang, Y. Wang, B. Zhu, F. Xia, C. Tung, J. Wu, H. Chen, J. Yu, Pt single atoms supported on N-doped mesoporous hollow carbon spheres with enhanced electrocatalytic H_2 -evolution activity, *Adv. Mater.* 33 (2021), 2008599.

[48] R.G.S. Pala, W. Tang, M.M. Sushchikh, J. Park, A.J. Forman, G. Wu, A. Kleiman-Shwarzstein, J. Zhang, E.W. McFarland, H. Metiu, CO oxidation by Ti- and Al-doped ZnO : oxygen activation by adsorption on the dopant, *J. Catal.* 266 (2009) 50–58.

[49] X. Liu, K. Zhou, L. Wang, B. Wang, Y. Li, Oxygen vacancy clusters promoting reducibility and activity of ceria nanorods, *J. Am. Chem. Soc.* 131 (2009) 3140–3141.

[50] Z. Hu, B. Li, X. Sun, H. Metiu, Chemistry of doped oxides: the activation of surface oxygen and the chemical compensation effect, *J. Phys. Chem. C* 115 (2011) 3065–3074.

[51] A. Suarez Negreira, J. Wilcox, Role of WO_3 in the hg oxidation across the $\text{V}_2\text{O}_5\text{-WO}_3\text{-TiO}_2$ SCR catalyst: a DFT study, *J. Phys. Chem. C* 117 (2013) 24397–24406.